Quantum Oscillations in Magnetothermopower Measurements of the Topological Insulator Bi$_2$Te$_3$

Dong-Xia Qu,[1,*] Y. S. Hor,[2] and R. J. Cava[3]

[1]*Lawrence Livermore National Laboratory, Livermore, California 94550, USA*
[2]*Department of Physics, Missouri University of Science and Technology, Rolla, Missouri 65409, USA*
[3]*Department of Chemistry, Princeton University, Princeton, New Jersey 08544, USA*

We report the magnetothermopower measurements of the nonmetallic topological insulator Bi$_2$Te$_3$ in magnetic fields up to 35 T. Quantum oscillations arising from surface states are observed in both thermoelectric and conductivity tensors. The inferred surface thermopower has a peak magnitude ~ 1 mV/K possibly as a result of surface electron and bulk phonon interaction. At the $n = 1$ Landau level, we resolve additional quantum oscillations signaling Landau sublevels.

Topological insulators (TIs) are a new class of quantum states of matter with topologically protected conducting surface states, arising from the topology of the bulk electronic band structure [1–5]. There are two distinguishing features of topological surface states. One is the existence of an odd number of Dirac cones on each surface, and the other is the helical spin arrangement [6–8]. Theoretically, the relativistic nature of Dirac fermions is believed to significantly modify the electron-electron interactions, with the possibility to produce more robust ground states at the $n = 1$ Landau level (LL) in Dirac fermions than in conventional two-dimensional (2D) electron systems [9–12]. The unique spin texture protects the topological surface states from nonmagnetic perturbations and $2k_F$ backscattering, making the surface mobility much higher than that of bulk.

To date, the topological surface states have been identified in a class of bismuth based compounds, such as Bi$_x$Sb$_{1-x}$, Bi$_2$Te$_3$, and Bi$_2$Se$_3$ by angle resolved photoemission spectroscopy [13–16]. Quantum oscillations of surface states have also been widely studied by transport experiments [17–24] and scanning tunneling microscopy [25,26]. However, most magnetoresistance measurements have been limited to samples with surface mobility below 3000 cm^2/V s [17,19–22,24] and the electrical surface conduction is susceptible to conducting bulk states.

Three-dimensional TIs including Bi$_2$Te$_3$, Bi$_2$Se$_3$, and Sb$_2$Te$_3$ are also excellent thermoelectircs, which have been intensively investigated for optimized thermoelectric performance in the past few decades [27,28]. However, previous thermoelectric measurements focused on metallic crystals, and the magnetothermoelectric transport of topological surfaces states has yet to be experimentally probed. In this Letter, we report the observation of quantum oscillations arising from surface states in the magnetothermopower measurement of nonmetallic Bi$_2$Te$_3$. In the high magnetic field, the surface thermopower displays an oscillation magnitude on the order of mV/K that is significantly higher than the bulk thermopower. When the filling factor

ν is less than 2, we find series of sharp peaks suggestive of Landau sublevels.

In the thermopower experiment, one end of the sample is held at the cold finger while the other end is anchored with a heater. To maximize the experimental accuracy, we used an alternating heat current at a low frequency of 67 mHz to produce an alternating temperature gradient measured with two thermocouple wires. Electrical contacts to the samples are made by gold wires using silver paste. One challenge for the thermopower measurement in a high magnetic field comes from the field dependence of the thermopower of voltage leads. To overcome this problem, we kept $\Delta T < 10$ mK across the voltage leads with the field swept at a rate of 0.4 T/min. Given that $S_{\mathrm{Au}} < 0.5$ μV/K at 7 K up to 30 T, the voltage drop from the Au wires is less than 5 nV in our measurements. The Hall and resistance measurements extended to 35 T were performed in the same cooldown with the thermopower measurements. We used a dc current under 300 μA with a field sweeping rate of 2 T/min.

We use the same batch of nonmetallic Bi$_2$Te$_3$ as that for high-field resistivity study [18]. Figure 1(a) shows the resistivity ρ_{xx} versus temperature profiles for representative samples $Q1$ and $Q2$. At 7 K, both samples display a weak-field Hall anomaly, which is a snapshot of high mobility surface conduction [Figs. 1(b) and 1(c)]. To determine the mobility μ_s of surface electrons, we fit the profile of Hall conductance G_{xy}^s [Fig. 1(d)] and find $\mu_s = 14100$ and 9500 cm^2/V s for samples $Q1$ and $Q2$, respectively.

We then examined the dependence of thermopower S_{xx} on temperature T in both metallic and nonmetallic crystals. When a temperature gradient $-\nabla T$ is applied along the sample, both charge carriers and phonons flow from hot to cold. The diffusion of charge carriers leads to a net electric field E^d which determines the diffusive thermopower $S^d = -E^d/|\nabla T|$. Meanwhile, the streaming phonons deliver part of the momentum to carriers and drag them to the cold end of the sample. The carrier accumulation builds up an electric field E^g which determines the phonon-drag
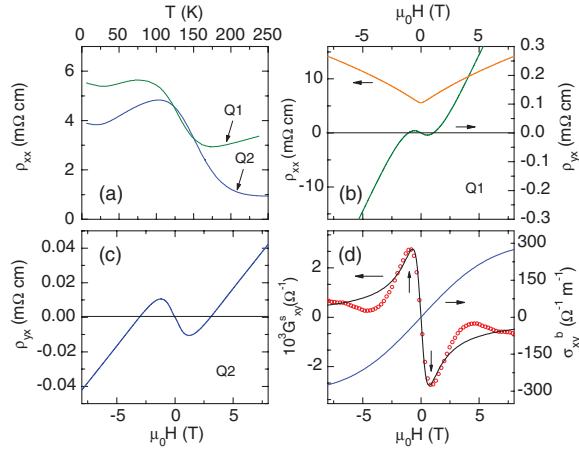
FIG. 1 (color). Hall mobility and carrier density characterization of nonmetallic Bi_2Te_3. (a) The resistivity ρ_{xx} versus temperature T profiles in samples $Q1$ and $Q2$ between 4 and 250 K. The sample size ($W \times L \times t$) is $750 \times 300 \times 50$ μm^3 for $Q1$ and $500 \times 275 \times 20$ μm^3 for $Q2$, where W is the width, L the length, and t the thickness. (b) ρ_{xx} and Hall resistivity ρ_{yx} versus H in sample $Q1$ at 7 K. Note that ρ_{yx} is displayed enlarged for clarity by a factor of 20 relative to ρ_{xx}. (c) The measured ρ_{yx} in sample $Q2$ at 7 K. (d) Surface Hall conductance G_{xy}^s (red circles) obtained by subtracting σ_{xy}^b from observed Hall conductivity $\sigma_{xy} = \rho_{yx}/(\rho_{xx}^2 + \rho_{yx}^2)$. The black curve is the fit to $G_{xy}^s = (2\pi e^3/h^2)\{Bl_e^2/[1 + (\mu_s B)^2]\}$, where l_e is the mean free path, h Planck's constant, e the electron charge, and μ_s the Hall mobility. In semiclassical treatment, μ_s is related to the metallicity parameter $k_F l_e$ as $\mu_s = el_e/\hbar k_F$. The blue curve is the calculated σ_{xy}^b from $\sigma_{xy}^b = p_{\text{eff}} e \mu_b \{\mu_b B/[1 + (\mu_b B)^2]\}$, where p_{eff} is the effective bulk carrier density and μ_b is the bulk mobility. The fit yields $\mu_s \sim 14000$ cm^2/V s.

thermopower $S^g = -E^g/|\nabla T|$. The total thermoelectric power S_{xx} is the sum of diffusive thermopower S^d and phonon-drag thermopower S^g. As shown in Fig. 2, insets, though S_{xx} shows a low-T peak in all these samples, the peak of the nonmetallic samples $Q1$ and $Q2$ is significantly stronger than that of the metallic sample $M1$. These observed peaks indicate the occurrence of the phonon-drag effect that is expected to appear at ~29 K in high purity Bi_2Te_3 crystals [29]. It has been demonstrated that the phonon-drag thermopower from a 2D conducting layer on a 3D crystal can display giant quantum oscillations due to the phonon intra- and inter-LL scattering in the presence of a strong magnetic field [30–32]. In such a 3D system, surface electrons are dragged by nonequilibrium 3D phonons of the whole specimen, while in a purely 2D system such as graphene, electrons of a wave vector k can only interact with 2D phonons of a wave vector $q \le 2k$. In addition, the bulk thermopower is considerably suppressed due to the existence of two types of bulk carriers with opposite signs [18]. Therefore, the thermopower measurement may provide a powerful tool to elucidate the nature of the topological surface states that is difficult to probe by the conductance measurement.
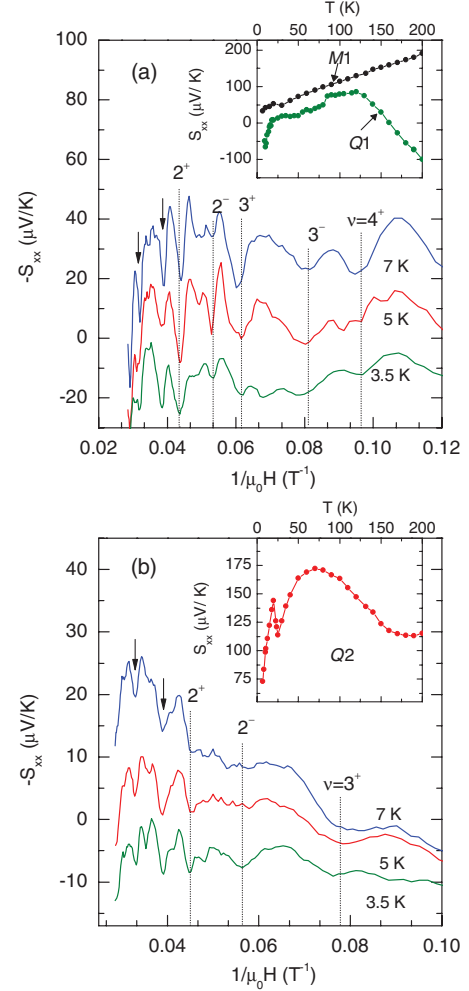

FIG. 2 (color). Magnetothermopower in high magnetic fields. (a) The thermopower response $-S_{xx}$ versus $1/H$ in sample $Q1$ at $T = 3.5, 5,$ and 7 K. (b) $-S_{xx}$ versus $1/H$ in sample $Q2$. The insets show the T dependence of the thermopower profiles in samples $Q1$ and $M1$ (a) and in sample $Q2$ (b). The arrows mark the subinteger dips resolved in $1/H < 0.06$ T^{-1}. The dashed lines indicate the oscillating minima in the low field regime.

Figures 2(a) and 2(b) show the thermopower response $-S_{xx}$ versus the inverse magnetic field $1/H$ in samples $Q1$ and $Q2$, respectively. Large LL oscillations begin to emerge at $H > 8$ T and their amplitude becomes smaller as T decreases from 7 to 3.5 K. An interesting feature of these oscillations is that at $1/H < 0.06$ T^{-1} sharp dips (black arrows) appear, with an aperiodic spacing smaller than the oscillating structure in the low field regime.

It is illuminating to compare the oscillations in $-S_{xx}$ and the Shubnikov–de Haas effect in the conductance tensor, which was confirmed to arise from the 2D surface states in the previous study [18]. As shown in Fig. 3, the extrema in $-\Delta S_{xx}$ coincide with the extrema in ΔG_{xx}, and are phase shifted by 90° from the extrema of $\Delta\rho_{yx}$. This occurs because both $-S_{xx}$ ($S_{xx} < 0$ for electronlike carriers) and σ_{xx} peak when the Fermi level (E_F) aligns with each LL,
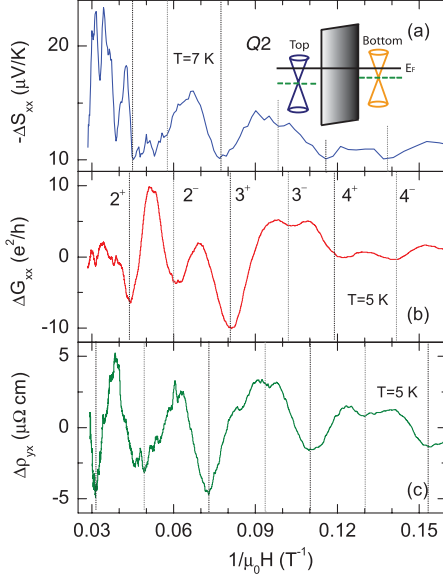
FIG. 3 (color). The quantum oscillations in $-\Delta S_{xx}$, ΔG_{xx}, and $\Delta\rho_{yx}$ in sample Q2. (a) $-\Delta S_{xx}$ is plotted as a function of $1/H$ at $T = 7$ K. (b) ΔG_{xx} versus $1/H$ at $T = 5$ K. (c) $\Delta\rho_{yx}$ versus $1/H$ at $T = 5$ K. A smooth background has been subtracted from three quantities. The vertical dashed lines mark the minima of $-\Delta S_{xx}$, ΔG_{xx}, and $\Delta\rho_{yx}$. The extrema of $-\Delta S_{xx}$ and ΔG_{xx} are in phase with each other, whereas they are phase shifted by 90° from the extrema of $\Delta\rho_{yx}$. The LL filling factor ν^s of the top (+) and bottom (−) Fermi surfaces are indexed in all panels.

whereas they vanish when E_F lies between LLs. Furthermore, we observe pronounced LL splitting near $1/H = 0.061, 0.102$, and 0.142 T^{-1} (gray dashed lines in Fig. 3). This splitting indicates that the degeneracy is lifted between top (+) and bottom (−) surfaces. A similar effect has been seen in strained HgTe 3D TIs [33], Bi$_2$Te$_3$ flakes [34], and Bi$_2$Se$_2$Te bulk crystals [22]. Here, a weak Te composition gradient in Bi$_2$Te$_3$ breaks the inversion symmetry and generates displaced Dirac points [see the inset of Fig. 3(a)]. By cleaving the crystal into bulk samples with a thickness $t = 20$–100 μm, we obtain slightly different surface carrier densities, which then leads to two sets of ν in one piece of sample. Hence, we can pinpoint the top and bottom surface index fields B_{ν^+} and B_{ν^-} from the periodic spacing of strong (black dashed lines) and weak (grey dashed lines) minima in ΔG_{xx} for sample Q2 [Fig. 3(b)]. Similar results were observed in sample Q1.

In terms of the carrier concentration n_e on one surface, B_ν is related to ν by

$$B_\nu = \frac{n_e\phi_0}{(\nu - \gamma)}, \qquad (1)$$

where $\phi_0 = h/e$ is the magnetic flux quanta, h is Planck's constant, e the charge of the electron, and γ the filling factor shift. A shift with $\gamma = 0$ corresponds to a conventional spectrum, whereas a deviation from the zero shift

with $\gamma = 1/2$ implies a Dirac spectrum. The $1/2$ arises from the $n = 0$ LL at the Dirac point. In the following, we label the filling factors as ν^s, where $s = \pm$ indexes the top and bottom surface states. With the $B_{\nu^s}^{-1}$ identified in both $-S_{xx}$, ΔG_{xx}, and $\Delta\rho_{yx}$, we plot them against ν [Figs. 4(a) and 4(b)]. The slopes of the linear fit to the data yield the carrier concentration $n_e = 7.37(5.92) \times 10^{11}$ cm^{-2}, with the Fermi wave vector $k_F = 0.030(0.027)$ Å^{-1}, for the top (bottom) surface states in sample Q2. The linear fit intercepts the ν axis at $\gamma = 0.67 \pm 0.05$ in Q2, close to $1/2$ instead of 0 or 1.

By fitting $\Delta G_{xx}(T)$ versus T with the expression $\Delta G_{xx}(T) = \Delta G_{xx}(0)\lambda/\sinh(\lambda)$ ($\lambda = 2\pi^2 k_B T/\hbar\omega_c$, where ω_c is the cyclotron frequency), we obtain the cyclotron

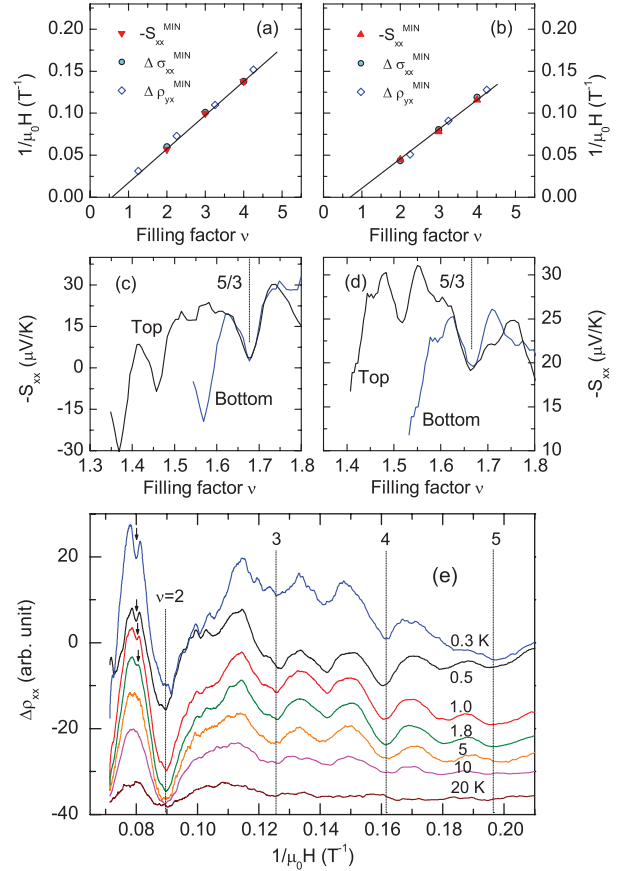FIG. 4 (color). The top panels show the $1/H$ positions of the $-S_{xx}$, ΔG_{xx}, and $\Delta\rho_{yx}$ minima versus the filling factor ν in sample Q2 for bottom surface (a) and top surface (b). The $1/H$ at minima of $\Delta\rho_{yx}$ is plotted against $\nu + \frac{1}{4}$. The middle panels show the $-S_{xx}$ as a function of the filling factor $\nu = n_e\phi_0 B^{-1} + \gamma$ in sample Q1 (c) and Q2 (d) at 7 K. For Q1, the index plot of oscillation extrema versus ν yields $n_e = 9.27$ and 7.61×10^{11} cm^{-2}, with $\gamma = 0.45 \pm 0.05$, for the top and bottom surfaces, respectively. The curves are vertically offset for clarity. The bottom panel shows $\Delta\rho_{xx}$ versus $1/H$ at selected T for sample Q3 ($t = 100$ μm). A subinteger dip (indicated by the arrow) at $1 < \nu < 2$ can be clearly resolved at 0.3 K, and it gradually diminishes to zero as $T > 1$ K.

mass $m_{cyc} = 0.085 m_e$, where m_e is the free-electron mass. With $k_F = 0.030$ Å^{-1}, we then calculate the Fermi velocity $v_F = 3.9 \times 10^5$ m/s, which is consistent with the angle resolved photoemission spectroscopy result [14]. Furthermore, the weak-field Hall anomaly provides an independent measurement of the average k_F. The value of k_F derived from surface Hall conductance is in reasonable agreement with the quantum oscillation analysis.

We next extract the surface thermopower S_{xx}^s from the observed thermopower response. In the experimental geometry with $-\nabla T \parallel \hat{\mathbf{x}}$, the total charge current density J is the sum of bulk current density J^b and surface current density J^s divided by the sample thickness t, viz.,

$$J = J^b + J^s/t, \qquad (2)$$

where $J_i^b = \sum_j [\sigma_{ij}^b E_j + \alpha_{ij}^b(-\partial_j T)]$ $(i = x, y)$, $J_i^s = \sum_j [G_{ij}^s E_j + \alpha_{ij}^s(-\partial_j T)]$ $(i = x, y)$, with σ_{ij}^b the bulk conductivity tensor, G_{ij}^s the surface conductance tensor, and α_{ij}^l ($l = b$ or s) the bulk or surface thermoelectric conductivity tensor. As the total conductivity tensor σ_{ij} is $\sigma_{ij} = \sigma_{ij}^b + G_{ij}^s/t$, J can be expressed as

$$J = \sum_j \left[\sigma_{ij} E_j + \left(\alpha_{ij}^b + \frac{\alpha_{ij}^s}{t} \right)(-\partial_j T) \right]. \qquad (3)$$

Because of the open boundary condition, we may obtain S via solving for $\mathbf{E}$ with $J = 0$,

$$S_{ij} = -E_i/\partial_j T = \sum_{k=x,y} \rho_{ik} \left(\alpha_{kj}^b + \frac{\alpha_{kj}^s}{t} \right), \qquad (4)$$

where ρ_{ij} is the total resistivity tensor. By setting $J^b = 0$ and $J^s = 0$, we may get α_{ij} from the thermopower tensor S_{ij} as $\alpha_{ij}^b = \sum_{k=x,y} \sigma_{ik}^b S_{kj}^b$ and $\alpha_{ij}^s = \sum_{k=x,y} G_{ik}^s S_{kj}^s$. Given that nonmetallic Bi$_2$Te$_3$ displays $\rho_{xx} \gg \rho_{yx}$, $\sigma_{xx}^b \gg \sigma_{xy}^b$, $G_{xx}^s \gg G_{xy}^s$, and $\sigma_{xx} \gg G_{xx}^s/t$ in high fields, S_{xx} may be approximated as

$$S_{xx} = S_{xx}^b + \frac{1}{t} \rho_{xx} G_{xx}^s S_{xx}^s, \qquad (5)$$

where S_{xx}^b is the bulk thermopower, which only gives rise to a featureless background. The $\rho_{xx} G_{xx}^s/t$ term can be obtained from the resistivity measurements. We find that the maximum magnitude of $\rho_{xx} G_{xx}^s/t \sim 0.027$ and 0.01 in $Q1$ and $Q2$, respectively. From Eq. (5), we can extract the peak magnitude of $-S_{xx}^s$, which is in the range of 0.5–2.0 mVK^{-1}, more than an order of magnitude higher than that of the bulk ~ 30 μVK^{-1} at 5 K. Unlike conventional 2D systems where the thermopower magnitude roughly displays a linear field dependence [30], the surface thermopower at higher order LLs such as $n = 4$ is comparable or even greater than that of lower LLs ($n = 3$). This giant oscillating magnitude and the specific field profile of the surface thermopower may be understood within the scenario of the 2D Dirac electron and 3D phonon interaction. Because of the relativistic dispersion of topological surface states, the wave function Ψ_n of a Dirac electron in the nth LL is the superposition of the nth and $(n - 1)$th LL wave functions of a nonrelativistic electron [9–11,35,36]. The mixture nature of the wave function significantly modifies the electron-phonon matrix element in the $n \geq 1$ LLs [32], leading to a thermopower profile different from an ordinary 2D system.

Besides integer Landau oscillations, we observe additional narrow, reproducible dips at $-S_{xx}$ in the range of $1 < \nu < 2$ for samples $Q1$ and $Q2$ [Figs. 2(a) and 2(b)]. Interestingly, if we plot the $-S_{xx}$ versus the filling factor calculated as $\nu = n_e \phi_0 B^{-1} + \gamma$, the $-S_{xx}(\nu)$ traces obtained at various n_e are almost overlapped, and their minima are all located around $\nu = \frac{5}{3} \pm 0.02$ [Figs. 4(c) and 4(d)]. The T dependence of $\Delta \rho_{xx}$ is shown for sample $Q3$ in Fig. 4(e). We find that the subinteger oscillation rapidly disappears as T is above 1 K, whereas the integer Landau oscillation sustains up to 20 K. There has been a report of fractional-filling states at $n = 1$ LL in (Bi$_{1-x}$Sb$_x$)$_2$Se$_3$, resolved in the second-derivative trace of a resistivity tensor [19]. Here, we show that the sublevel oscillations are directly evident in the raw trace of $-S_{xx}$. Their origin is the subject of ongoing research.

In summary, we report the thermopower measurement of nonmetallic TI in the presence of a high magnetic field. Quantum oscillations in the thermoelectric tensor are consistent with Shubnikov-de Haas oscillations arising from topological surface states. The observed surface magnetothermopower is significantly higher than the bulk values. With its sensitivity to surface states, thermopower may provide a useful tool to study quantum transport in TIs.

*qu2@llnl.gov

[1] C. L. Kane and E. J. Mele, Phys. Rev. Lett. **95**, 146802 (2005).

[2] B. A. Bernevig and S.-C. Zhang, Phys. Rev. Lett. **96**, 106802 (2006).

[3] J. E. Moore and L. Balents, Phys. Rev. B **75**, 121306(R) (2007).

[4] L. Fu and C. L. Kane, Phys. Rev. B **76**, 045302 (2007).

[5] X.-L. Qi, T. L. Hughes, and S.-C. Zhang, Phys. Rev. B **78**, 195424(R) (2008).

[6] P. Roushan, J. Seo, C. V. Parker, Y. S. Hor, D. Hsieh, D. Qian, A. Richardella, M. Z. Hasan, R. J. Cava, and A. Yazdani, Nature (London) **460**, 1106 (2009).

[7] M. Z. Hasan and C. L. Kane, Rev. Mod. Phys. **82**, 3045 (2010).

[8] X.-L. Qi and S.-C. Zhang, Rev. Mod. Phys. **83**, 1057 (2011).

[9] M. O. Goerbig, R. Moessner, and B. Doucot, Phys. Rev. B **74**, 161407 (2006).

[10] K. Yang, S. Das Sarma, and A. H. MacDonald, Phys. Rev. B **74**, 075423 (2006).

[11] V. M. Apalkov and T. Chakraborty, Phys. Rev. Lett. **97**, 126801 (2006).

[12] C. Toke, P. Lammert, V. Crespi, and J. Jain, Phys. Rev. B **74**, 235417 (2006).

[13] D. Hsieh et al., Science **323**, 919 (2009).

[14] Y. L. Chen et al., Science **325**, 178 (2009).

[15] Y. Xia et al., Nat. Phys. **5**, 398 (2009).

[16] D. Hsieh, D. Qian, L. Wray, Y. Xia, Y. S. Hor, R. J. Cava, and M. Z. Hasan, Nature (London) **452**, 970 (2008).

[17] A. A. Taskin and Y. Ando, Phys. Rev. B **80**, 085303 (2009).

[18] D.-X. Qu, Y. S. Hor, J. Xiong, R. J. Cava, and N. P. Ong, Science **329**, 821 (2010).

[19] J. G. Analytis, R. D. McDonald, S. C. Riggs, J.-H. Chu, G. S. Boebinger, and I. R. Fisher, Nat. Phys. **6**, 960 (2010).

[20] Z. Ren, A. Taskin, S. Sasaki, K. Segawa, and Y. Ando, Phys. Rev. B **82**, 241306 (2010).

[21] A. A. Taskin, Z. Ren, S. Sasaki, K. Segawa, and Y. Ando, Phys. Rev. Lett. **107**, 016801 (2011).

[22] J. Xiong, A. C. Petersen, D. Qu, Y. S. Hor, R. J. Cava, and N. P. Ong, Physica (Amsterdam) **44**, 917 (2012).

[23] L. He et al., Nano Lett. **12**, 1486 (2012).

[24] A. A. Taskin, S. Sasaki, K. Segawa, and Y Ando, Phys. Rev. Lett. **109**, 066803 (2012).

[25] P. Cheng et al., Phys. Rev. Lett. **105**, 076801 (2010).

[26] T. Hanaguri, K. Igarashi, M. Kawamura, H. Takagi, and T. Sasagawa, Phys. Rev. B **82**, 081305(R) (2010).

[27] H. Scherrer and S. Scherrer, in Handbook of Thermoelectrics, edited by D. M. Rowe (CRC Press, New York, 1996), pp. 211–237.

[28] Y. S. Hor, A. Richardella, P. Roushan, Y. Xia, J. G. Checkelsky, A. Yazdani, M. Z. Hasan, N. P. Ong, and R. J. Cava, Phys. Rev. B **79**, 195208 (2009).

[29] P. A. Walker, Proc. Phys. Soc. London **76**, 113 (1960).

[30] R. Fletcher, J. C. Maan, K. Ploog, and G. Weimann, Phys. Rev. B **33**, 7122 (1986).

[31] B. Tieke, U. Zeitler, R. Fletcher, S. A. J. Wiegers, A. K. Geim, J. C. Maan, and M. Henini, Phys. Rev. Lett. **76**, 3630 (1996).

[32] S. K. Lyo, Phys. Rev. B **40**, 6458 (1989).

[33] C. Brüne, C. X. Liu, E. G. Novik, E. M. Hankiewicz, H. Buhmann, Y. L. Chen, X. L. Qi, Z. X. Shen, S. C. Zhang, and L. W. Molenkamp, Phys. Rev. Lett. **106**, 126803 (2011).

[34] M. Veldhorst et al., Nat. Mater. **11**, 417 (2012).

[35] A. M. DaSilva, Solid State Commun. **151**, 1444 (2011).

[36] C.-X. Liu, X.-L. Qi, H. Zhang, X. Dai, Z. Fang, and S.-C. Zhang, Phys. Rev. B **82**, 045122 (2010).